Featured Article

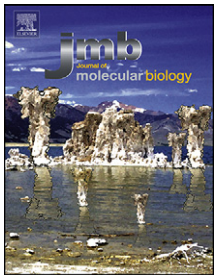

Steric Mechanism of Auto-Inhibitory Regulation of Specific and Non-Specific DNA Binding by the ETS Transcriptional Repressor ETV6

Soumya De[1], Anson C.K. Chan[2], H. Jerome Coyne III[1], Niraja Bhachech[3,4], Ulrike Hermsdorf[1], Mark Okon[1], Michael E.P. Murphy[2], Barbara J. Graves[3,4] and Lawrence P. McIntosh[1]

1 - Department of Biochemistry and Molecular Biology, Department of Chemistry, and Michael Smith Laboratories, *University of British Columbia, Vancouver, BC, Canada V6T 1Z3*
2 - Department of Microbiology and Immunology, *University of British Columbia, Vancouver, BC, Canada V6T 1Z3*
3 - Department of Oncological Sciences, *University of Utah School of Medicine, and Huntsman Cancer Institute, University of Utah, Salt Lake City, UT 84112–5550, USA*
4 - Howard Hughes Medical Institute, *Chevy Chase, MD 20815–6789, USA*

Correspondence to Lawrence P. McIntosh: *mcintosh@chem.ubc.ca*
http://dx.doi.org/10.1016/j.jmb.2013.11.031
Editor by C. Kalodimos

Soumya De, Barbara J. Graves, and Lawrence P. McIntosh

Abstract

DNA binding by the ETS transcriptional repressor ETV6 (or TEL) is auto-inhibited ~50-fold due to an α-helix that sterically blocks its ETS domain binding interface. Using NMR spectroscopy, we demonstrate that this marginally stable helix is unfolded, and not displaced to a non-inhibitory position, when ETV6 is bound to DNA containing a consensus $^{5'}$GGAA$^{3'}$ recognition site. Although significantly lower in affinity, binding to non-specific DNA is auto-inhibited ~5-fold and is also accompanied by helix unfolding. Based on NMR chemical shift perturbations, both specific and non-specific DNA are bound via the same canonical ETS domain interface. However, spectral perturbations are smaller for the non-specific complex, suggesting weaker and less well-defined interactions than in the specific complex. In parallel, the crystal structure of ETV6 bound to a specific DNA duplex was determined. The structure of this complex reveals that a non-conserved histidine residue in the ETS domain recognition helix helps establish the specificity of ETV6 for DNA-binding sites containing $^{5'}$GGAA$^{3'}$ *versus* $^{5'}$GGAT$^{3'}$. These studies provide a unified steric mechanism for attenuating ETV6 binding to both specific and non-specific DNA and expand the repertoire of characterized auto-inhibitory strategies utilized to regulate ETS factors.

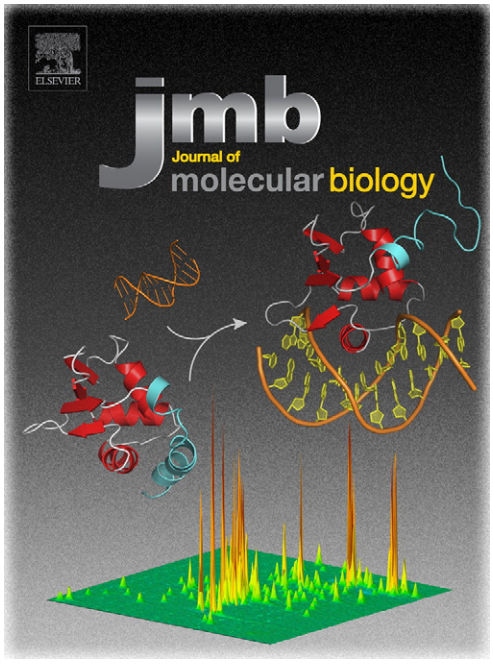

Legend. The transcriptional repressor ETV6 is auto-inhibited by a helical C-terminal inhibitory domain (cyan) that sterically blocks the DNA-binding surface of its ETS domain (red). Upon binding both specific and non-specific DNA sequences, an inhibitory helix unfolds, yielding the sharp strong signals in the ^{15}N heteronuclear single quantum correlation spectrum of the bound protein.

Introduction

Auto-inhibition is a powerful "on-site" regulatory mechanism used to modulate a wide variety of biomolecular interactions [1]. The ETS family of transcription factors displays several examples of DNA-binding auto-inhibition [2]. These proteins are defined by the conserved ETS domain, which recognizes very similar DNA sequences containing a core $^{5'}$GGA(A/T)$^{3'}$ motif [3]. One role of controlling DNA binding by auto-inhibition is to provide added specificity for targeting distinct ETS proteins to appropriate transcriptional regulatory sequences. The relief of ETS-1 auto-inhibition through cooperative DNA binding with RUNX1, a frequently occurring partnership in T cell enhancers, exemplifies such added specificity [2,4].

We seek to understand the common and distinct mechanisms of auto-inhibition within the ETS family in order to gain a deeper insight into the evolution of DNA-binding control to achieve biological specificity. In the case of the prototypic member ETS-1, there is an extensive structural and dynamic understanding of its auto-inhibition. A combination of steric and allosteric mechanisms that integrate various signaling events have been uncovered, such as post-translational modifications and partner-protein interactions, resulting in both negative and positive control of ETS-1, respectively [4–6]. Briefly, ETS-1 auto-inhibition is mediated by a set of helices that flank its ETS domain. This inhibitory module is distal from the DNA-binding interface and, upon DNA binding, undergoes an allosteric conformational change highlighted by the unfolding of a marginally stable helix [7,8]. Additionally, an adjacent intrinsically disordered serine-rich region (SRR) plays a critical role in the Ca^{2+}-dependent, phosphorylation-enhanced auto-inhibition of ETS-1 by stabilizing the inhibitory module and by transiently masking its DNA-binding interface [6,9]. A second ETS member, ERG, has also been recently shown to be modestly auto-inhibited by a flexible sequence N-terminal to its ETS domain [10]. In contrast, the mechanisms by which most other ETS proteins are auto-inhibited are not well understood.

In this study, we extended our investigation of regulation by auto-inhibition to ETV6 (or TEL, *t*ranslocation *E*TS *l*eukemia). Unlike the transcriptional activators ETS-1 and ERG, ETV6 is a repressor [11]. Furthermore, it also self-associates due to the presence of a PNT (or SAM) domain, thereby facilitating cooperative binding on tandem ETS DNA-binding sites for repressive activity [12–15]. Previously, we mapped an ETV6 inhibitory region C-terminal to its ETS domain [15]. This CID (*C*-terminal *i*nhibitory *d*omain) contains two helices, of which helix H5 sterically blocks the canonical ETS DNA-binding interface and thereby reduces its affinity for specific sequences by ~50-fold [15,16]. Similar to ETS-1, the inhibitory helices are marginally stable and their presence dampens dynamics of the ETS domain [16]. Preliminary evidence suggesting a conformational change accompanying DNA contact was provided by the relief of ETV6 auto-inhibition due to mutations that potentially disrupt the CID [15]. Thus, the central goal of this current study was to determine the conformational changes occurring in the ETV6 ETS domain and the CID upon DNA binding. We also investigated how the CID impacts both specific and non-specific DNA binding because binding a limited number of specific target sites in the cell occurs against a very high background of non-specific interactions.

We used a set of complementary NMR experiments to demonstrate that residues forming the inhibitory helix H5 are unfolded when ETV6 is bound to DNA. In parallel, with isothermal titration calorimetry (ITC) and NMR spectroscopy, we investigated the impact of CID on the interaction of ETV6 with non-specific DNA lacking the ETS consensus motif. Non-specific binding, which is substantially lower in affinity, is also auto-inhibited and is accompanied by helical unfolding. We further show that ETV6 utilizes a similar binding interface for both specific and non-specific DNA sequences. However, the non-specific complex appears relatively "loose" in comparison to the tight specific complex. To better define this interface, we determined the free and DNA-bound structures of the uninhibited ETV6 ETS domain with NMR spectroscopy and X-ray crystallography, respectively. The DNA-bound structure also helps explain the role of a non-conserved histidine in the preferential binding of ETV6 to the core sequence $^{5'}$GGAA$^{3'}$. Collectively, our studies uncover a unified steric mechanism of auto-inhibition that impacts both non-specific and specific DNA binding by an ETS protein.

Results

Helix H5 in CID unfolds when ETV6 binds to specific DNA

Structures of several ETS proteins show a highly conserved mode of DNA binding whereby the recognition helix H3 inserts into the major groove and makes extensive contacts with the $^{5'}$GGA(A/T)$^{3'}$ motif [2]. A similar canonical mode of binding by ETV6 would require that the CID must be either unfolded or otherwise displaced to remove steric blockage of the ETS domain. We tested this hypothesis by several complementary NMR experiments. Initially, we utilized ^{15}N heteronuclear single quantum correlation (HSQC) spectroscopy to monitor the interaction of ^{15}N-labeled ETV6^{D446} with a 15-bp oligonucleotide (DNA^{sp}) containing the ETS

consensus motif $^{5'}$GGAA$^{3'}$ (see Table 1 for nomenclature). Upon titration, peaks corresponding to the free protein diminished and a new set of signals corresponding to the bound state emerged (Fig. 1a and Supplemental Fig. S1). Such binding in the slow exchange regime is consistent with the relatively high nanomolar affinity of inhibited ETV6 for the consensus DNA sequence [16]. The chemical shifts of the ETV6^{D446}–DNA^{sp} complex were used to predict its backbone structure (Fig. 2a). This indicated that the ETS domain and the CID helix H4 retained the same secondary structure as in the unbound protein [16]. In contrast, residues corresponding to helix H5 displayed large ^{15}N-HSQC chemical shift perturbations (CSPs) and resulting chemical shifts diagnostic of a disordered polypeptide chain (Figs. 1b and 2a). In addition, these residues exhibited low order parameters (S^2) based on the "random coil index" [18].

To more directly characterize the dynamic properties of the ETV6^{D446}–DNA^{sp} complex, we also collected amide ^{15}N T_1, T_2 and heteronuclear nuclear Overhauser enhancement (NOE) relaxation data (Supplemental Fig. S2). From T_1/T_2 ratios, the global isotropic tumbling correlation time was determined to be 12.5 ± 0.2 ns. This is consistent with the 23-kDa molecular mass of the ETV6^{D446}–DNA^{sp} complex [19] and confirms that it is monomeric under the experimental conditions. More importantly, the ^{15}N-NOE values, which are very sensitive to the sub-nanosecond timescale motions of the amide ^{15}N–^{1}H^{N} bond vector, provide a measure of the fast local backbone dynamics of a protein. These data revealed a well-folded core ETS domain with high ^{15}N-NOE values yet a highly flexible CID with substantially lower values indicative of pronounced conformational mobility (Fig. 2b). An analysis of the full set of amide ^{15}N relaxation data according to the model-free formalism [20,21] similarly showed that the CID residues are dynamic with substantially lower conventional order parameters than those of the ETS domain (Supplemental Fig. S2).

Finally, we determined the tertiary structure of ETV6^{D446} bound to DNA^{sp} using NMR spectroscopy. Extensive ^{1}H, ^{13}C and ^{15}N chemical shift assignments, along with backbone dihedral angle and inter-proton NOE distance restraints for the protein component of the ETV6^{D446}–DNA^{sp} complex, were obtained by heteronuclear NMR experiments based on transverse relaxation optimized spectroscopy (Table 2). Although detected, the ^{1}H signals from the unlabeled DNA were not assigned. Using these data, we calculated the structural ensemble of the bound protein (Fig. 3a). Overall, the protein adopts the winged helix–turn–helix (wHTH) fold characteristic of ETS domains and closely resembles the structure of free auto-inhibited ETV6 ETS domain [16]. However, in marked contrast to a well-folded helix H5 blocking the binding interface of the unbound protein, the corresponding CID residues are disordered in the complex with high rmsd values. This is consistent with their dynamic nature and hence lack of any structural restraints. Collectively, chemical shift, ^{15}N relaxation and structural data clearly demonstrate that helix H5 unfolds upon specific DNA binding and is not simply displaced as an intact helix to an alternative position that is no longer auto-inhibitory.

Table 1. ETV6 constructs and DNA sequences

Name	Sequence	Comment
ETV6^{R426}	G329-R426	Uninhibited ETV6[a]
ETV6^{D446}	G329-D446	Inhibited ETV6[a]
ETV6$^{D446'}$	R335-D446	Inhibited ETV6[a]
ETV6^{R458}	R335-R458	Inhibited ETV6[a]
DNA^{sp}	5′-CAAGCC**GGAA**GTGAG-3′ 3′-GTTCGG**CCTT**CACTC-5′	Specific DNA[b]
DNA$^{sp\text{-}cryst}$	5′-AAAGCC**GGAA**GTGAG-3′ 3′- TTCGG**CCTT**CACTCT-5′	Specific DNA[b]
DNA^{nonsp}	5′-GATGCAGTGTAGTCG-3′ 3′-CTACGTCACATCAGC-5′	Non-specific DNA
DNA$^{sp\text{-}emsa\text{-}1}$	5′-CAAGCC**GGAA**GTGAG-3′ 3′-GTTCGG**CCTT**CACTC-5′	Specific DNA[b]
DNA$^{sp\text{-}emsa\text{-}2}$	5′-CAAGCC**GGAT**GTGAG-3′ 3′-GTTCGG**CCTA**CACTC-5′	Specific DNA[b]

[a] The core ETS domain spans Leu337 to Phe415, and helix H4 is formed by Pro419 to Ser424.
[b] The core $^{5'}$GGAA$^{3'}$ or $^{5'}$GGAT$^{3'}$ binding motif is in boldface.

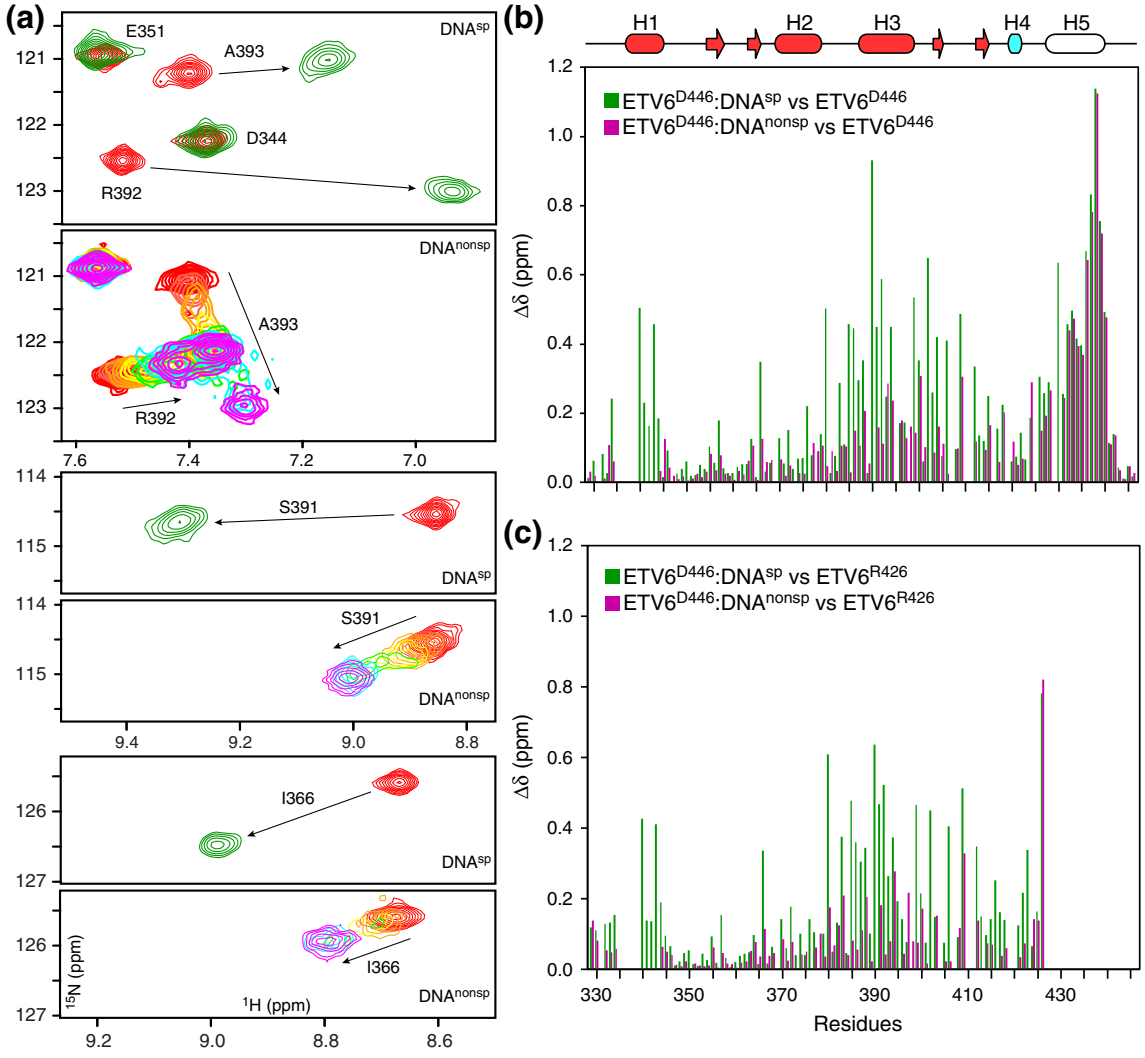

Fig. 1. NMR monitored titrations of ETV6 fragments with DNA. (a) Overlaid regions of the ^{15}N-HSQC spectra of ETV6^{D446} recorded in the absence (red) or in the presence of a 1.1 molar ratio of DNA^{sp} (green). High-affinity binding occurs in the slow exchange regime and only signals from the free or bound protein are detected at intermediate molar ratios (data not shown). Also shown are the same spectral regions when ETV6^{D446} is titrated with DNA^{nonsp} in molar ratios of 0 (red), 0.1, 0.25, 0.5, 0.75, 1, 2 and 3 (magenta). With weaker affinity, binding occurs in the fast exchange regime and signals progressively change from the chemical shift of the free to the DNA-bound state. Some broadening also occurs at intermediate saturation. See Supplemental Fig. S1 for the full spectra. (b) Amide CSPs ($\Delta\delta = \{\Delta\delta_H^2 + (0.154\Delta\delta_N)^2\}^{1/2}$) for ETV6^{D446}–DNA^{sp} (green) and ETV6^{D446}–DNA^{nonsp} (magenta) with respect to free ETV6^{D446}. The unfolding of helix H5 leads to large CSPs of similar magnitude for residues 430–440 in both complexes. In contrast, the CSPs for the ETS domain result from the displacement of helix H5 and the binding of DNA. In (c), the effects of helix H5 unfolding are removed by calculating CSPs relative to unbound ETV6^{R426}, which lacks this helix. Note that these CSPs were calculated using the chemical shifts of ETV6^{D446} in the presence of a 1.1-fold molar excess of DNA^{sp} and 3-fold molar excess of DNA^{nonsp} and thus correspond to 99% and 98% saturation, respectively, based on their respective K_D values and binding site sizes. The secondary structure (helix, cylinder; strand, arrow) is displayed as cartoon on top with the core ETS domain in red and helix H4 of the CID in cyan. Helix H5, which is unfolded in both complexes, is not colored.

ETV6 binding to non-specific DNA is also auto-inhibited

Using ITC and NMR spectroscopy, we also investigated the interaction of ETV6^{D446} and ETV6^{R426} (lacking helix H5) with a 15-bp non-specific DNA oligonucleotide (DNA^{nonsp}; Table 1). In contrast to the case of specific binding, for which there is one single high-affinity site within DNA^{sp}, ETV6 can potentially bind DNA^{nonsp} in numerous positions and in either orientation. Therefore, the measured ITC binding isotherms were fit to a variation of the McGhee–von Hippel model [22] developed by Record *et al.* [23] for non-specific

binding with neighbor exclusion to a finite lattice. As summarized in Fig. 4, this yielded the average microscopic dissociation constant (K_D), binding enthalpy (ΔH) and the effective binding site size (n). Both ETV6^{D446} and ETV6^{R426} bound DNA^{nonsp} with K_D values in the micromolar range, which is 10^3-fold to 10^4-fold weaker than their affinities to a specific oligonucleotide [15,16]. Most importantly, the K_D value for ETV6^{D446} is ~5-fold higher than that of ETV6^{R426}. Thus, binding to non-specific DNA by the ETV6 ETS domain is also auto-inhibited, albeit to a lesser extent than to specific DNA (~50-fold).

It is interesting to compare the differences in the binding site size between the specific and non-specific complexes. As described below, the crystal structure of ETV6 bound to specific DNA revealed that the protein contacts ~10 nucleotide pairs. In contrast, fitting of the ITC isotherms indicated that ETV6^{R426} and ETV6^{D446} effectively bind only 5.2 and 6.5 nucleotide pairs, respectively, in DNA^{nonsp}. These n values reflect the average site size (~6 bp) occluded by one ETV6 along the non-specific DNA duplex. Therefore, the first ETV6 molecule could potentially bind in either orientation to the 15-bp oligonucleotide at 10 (15 – 6 + 1) overlapping sites. However, due to neighbor exclusion, only two to three protein molecules bind one oligonucleotide under saturating conditions. This could be accommodated by adopting staggered rotated positions along the double helix. Parenthetically, these non-integral values likely arise from the violation of the key premises in the Record model that the DNA lattice consists of identical binding sites and that the protein has only one mode of binding [24]. Also, since DNA^{nonsp} contains many potential binding sites, fitting these ITC data to a simple isotherm yielded apparent, overall macroscopic K_D values ~10-fold lower than the microscopic values presented in Fig. 4 (data not shown). Importantly, regardless of model, auto-inhibited ETV6^{D446} binds to DNA^{nonsp} with ~5-fold weaker affinity than uninhibited ETV6^{R426}.

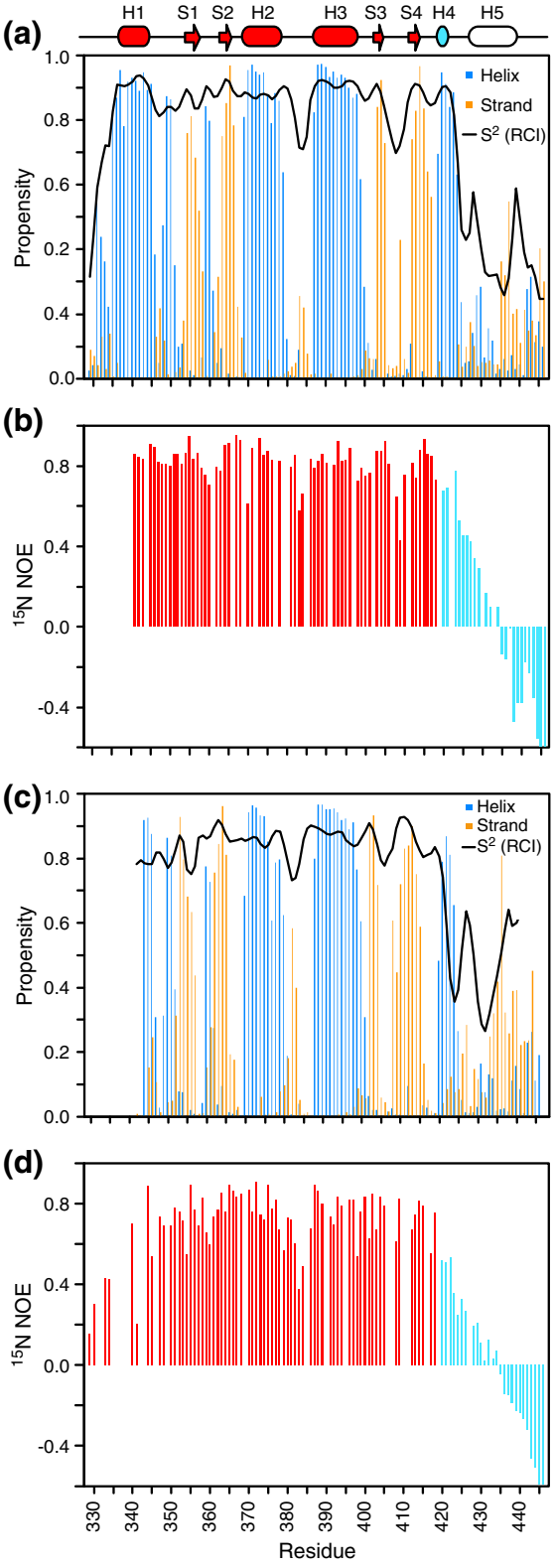

Fig. 2. Helix H5 is unstructured in both specific and non-specific ETV6–DNA complexes. The normalized secondary structure propensities (helices, blue; strands, orange) and random coil index (RCI) order parameters (S^2, black line) for the (a) ETV6^{D446}–DNA^{sp} and (c) ETV6^{D446}–DNA^{nonsp} complexes were calculated from $^{13}C^{\alpha}$, $^{13}C^{\beta}$, ^{15}N and $^{1}H^{N}$ chemical shifts using the program MICS [17]. The ^{15}N-NOE data for (b) ETV6^{D446}–DNA^{sp} and (d) ETV6^{D446}–DNA^{nonsp} are shown for the core ETS domain (red) and CID (cyan) residues. Decreasing NOE and S^2 values indicate increasing amide mobility on the sub-nanosecond timescale and thus show that helix H5 is unfolded in both complexes (see also Supplemental Fig. S2). The histogram bars for the two C-terminal residues are truncated, and missing data corresponds to prolines and residues with overlapping or unassigned signals. The top cartoon shows the secondary structural elements (helix, cylinder; strand, arrow) of the free inhibited ETS domain (red) and CID (cyan or not colored).

Table 2. NMR refinement statistics for protein structures

	$ETV6^{R426}$	$ETV6^{D446}$–DNA^{sp}
NMR distance and dihedral restraints		
Distance restraints		
Total NOE	1620	1540
Intra-residue	467	464
Inter-residue	1153	1076
Sequential ($\|i-j\|=1$)	382	459
Medium-range ($\|i-j\|\leq 4$)	285	271
Long-range ($\|i-j\|\geq 5$)	486	346
Dihedral angle restraints		
φ, ψ	85, 88	82, 84
Structure statistics		
Violations (mean ± SD)		
Distance restraints (Å)	0.06 ± 0.02	0.16 ± 0.13
Dihedral angle restraints (º)	4.72 ± 1.92	5.50 ± 2.08
Max. dihedral angle violation (º)	6.09	10.25
Max. distance restraint violation (Å)	0.42	0.32
Deviations from idealized geometry		
Bond lengths (Å)	0.005	0.005
Bond angles (º)	0.742	0.774
Impropers (º)	2.13	2.51
Average pairwise rmsd[a] (Å)		
All heavy atoms	1.03 ± 0.09	1.21 ± 0.12
Backbone only	0.59 ± 0.08	0.74 ± 0.11

[a] Pairwise rmsd was calculated among 10 refined structures for the residues 337–415.

Helix H5 also unfolds when ETV6 interacts with non-specific DNA

Complementing ITC, we used NMR spectroscopy to obtain structural details of the ETV6–DNA^{nonsp} interaction. Upon titration with DNA^{nonsp}, numerous amide ^{15}N–$^{1}H^{N}$ signals of $ETV6^{D446}$ showed progressive chemical shift changes (Fig. 1a and Supplemental Fig. S1). This is diagnostic of fast exchange between the free and bound forms of the protein and is consistent with a micromolar dissociation constant. Furthermore, only one signal per amide was observed in the ^{15}N-HSQC spectrum of the saturated $ETV6^{D446}$–DNA^{nonsp} complex (Supplemental Figs. S1 and S3). Thus, translocation of the bound protein between the many possible non-specific sites along this oligonucleotide is also fast on the chemical shift timescale.

Insights into the structure of the bound protein could be obtained from its assigned NMR spectra. Based on its main-chain chemical shifts, the $ETV6^{D446}$ ETS domain retained its wHTH secondary structure when bound to DNA^{nonsp} (Fig. 2c). In contrast, large CSPs occurred for residues corresponding to helix H5, suggesting a significant conformational change (Fig. 1b). Indeed, both chemical shift and ^{15}N relaxation measurements demonstrated that, as with DNA^{sp}, the CID adopted a dynamic random coil conformation in the ETV6–DNA^{nonsp} complex (Fig. 2c and d).

ETV6 binds non-specific DNA via the canonical ETS domain interface

The CSPs also revealed that the ETV6 ETS domain binds non-specific and specific DNA sequences via the same general interface. For this analysis, it is important to recognize that the spectral perturbations reflect both the unfolding of helix H5, which sterically blocks this interface, and the interactions with DNA (Fig. 1b and Supplemental Fig. S4). Accordingly, to focus only on the latter, we calculated the CSPs for the $ETV6^{D446}$–DNA^{sp} and $ETV6^{D446}$–DNA^{nonsp} complexes relative to free $ETV6^{R426}$, which lacks the CID helix H5. These CSPs are presented as the magnitude of the combined amide $^{1}H^{N}$ and ^{15}N changes in Fig. 1c and separately (with upfield or downfield "direction") for the two nuclei in Supplemental Fig. S5. For both complexes, residues in helix H3, the turn between helices H2 and H3 and the wing between S3 and S4 experienced the largest CSPs. When mapped onto the structure of ETV6 (Fig. 5), these residues cluster to the DNA-binding interface that has been well characterized in many ETS domain complexes [25]. Amide chemical shifts are exquisitely sensitive to their environment. Thus, CSPs may arise due to proximity to the charged and aromatic moieties in DNA, as well as from local or propagated conformational changes, such as those influencing hydrogen-bonding networks. Regardless of the exact cause, the similar patterns of CSPs demonstrate that $ETV6^{D446}$ uses the same canonical interface to bind both specific and non-specific DNA.

Paralleling their relative binding affinities, the CSPs for many residues were in the same approximate direction [26], yet smaller in magnitude, for the DNA^{nonsp} complex than for the DNA^{sp} complex (Figs. 1 and 5 and Supplemental Fig. S5). Comparable patterns of relative NMR spectral changes have been reported for the HMG-box [27] and ZNF217 zinc finger [28] proteins bound to non-specific *versus* specific DNA oligonucleotides. This is not a trivial result of incomplete saturation of the $ETV6^{D446}$–DNA^{nonsp} complex, as the protein was ~98% bound (Supplemental Fig. S3). Rather, this indicates that $ETV6^{D446}$ forms generally similar, albeit less well-defined, time-averaged interactions with DNA^{nonsp} than with DNA^{sp}. Such interactions likely involve electrostatic contacts between the positively-charged DNA-binding interface of $ETV6^{D446}$ and the negatively-charged phosphodiester backbone of DNA^{nonsp}, rather than base-specific hydrogen bonds. Also, rapid exchange between binding sites along DNA^{nonsp} should lead to smaller net CSPs due to averaging of potential positive and negative chemical shift changes.

Residue-wise comparison of the CSPs revealed potentially important structural differences between the two complexes (Figs. 1 and 5 and Supplemental Fig. S5). For example, Arg392 and His396, whose side chains interact with DNA bases in the ETV6–

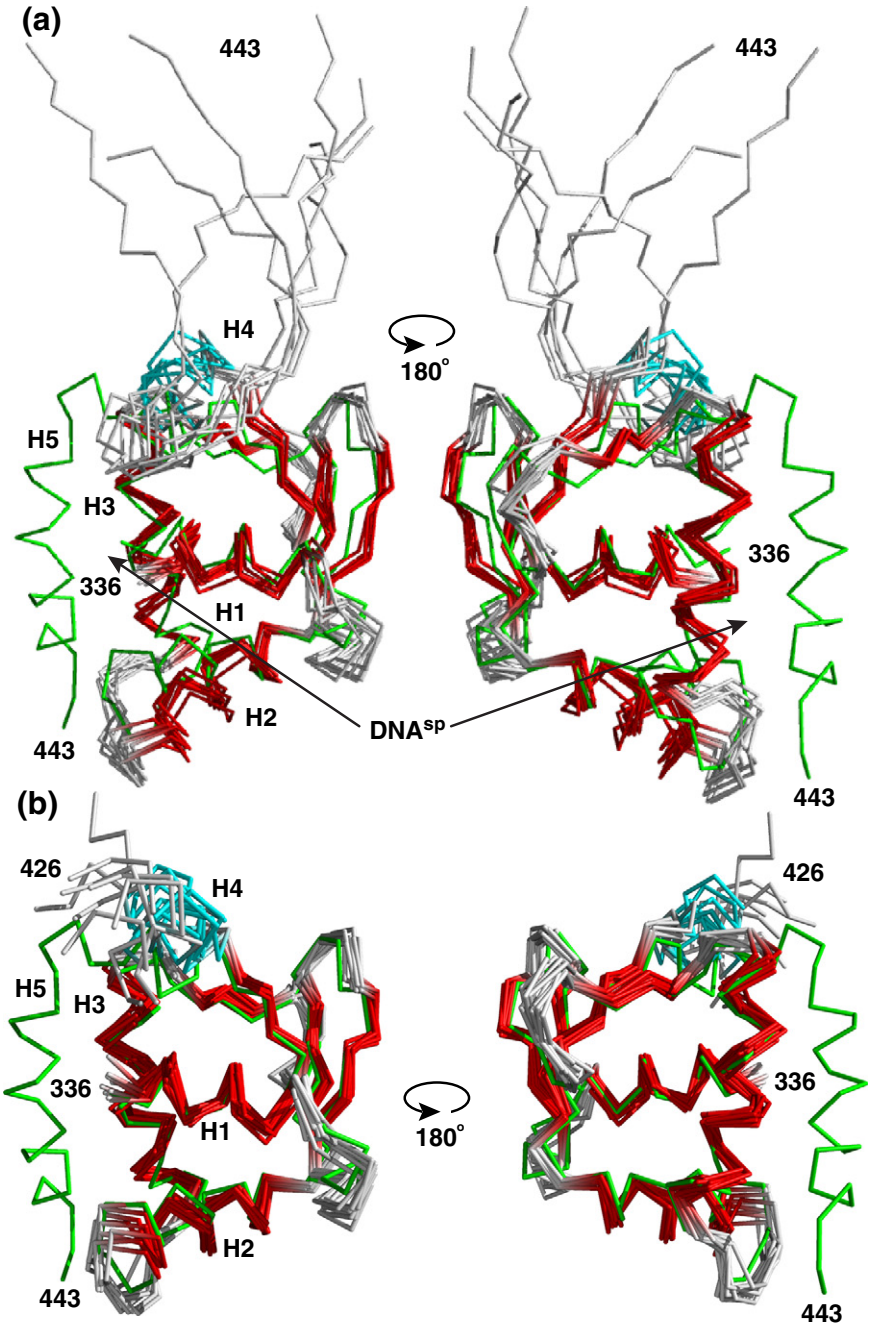

Fig. 3. Structural ensembles of free and bound ETV6 are similar except for the unfolding of helix H5. The NMR-derived structural ensembles of (a) the ETV6^{D446}–DNA^{sp} complex (ETS domain helices and strands, red; CID helix H4, cyan) and (b) uninhibited ETV6^{R426} align closely to the lowest-energy structure of inhibited ETV6^{R458} (green) [16]. CID helix H5, which blocks the DNA-binding interface of ETV6^{R458}, is absent in ETV6^{R426} and unfolded in the ETV6^{D446}–DNA^{sp} complex. Although present in the latter complex, DNA^{sp} was not included in the structure calculations. The N-terminal Gly-Ser-His-Met and unstructured residues (329–335 and 444–446) are not shown for clarity. Arrows point to the DNA-binding interface along helix H3.

DNA crystal structure (see below), experienced substantial CSPs in the specific complex, yet smaller perturbations with DNA^{nonsp}. Five additional lysine and arginine side chains, which interact with the phosphodiester backbone of DNA, also showed large amide CSPs in the specific complex, whereas only two (Lys380 and Arg382) exhibited substantial perturbations in the non-specific complex. In contrast, the ^{15}N chemical shift of Ala393, a residue in helix H3, changed with opposite sign upon binding

(a)

	$ETV6^{D446}$	$ETV6^{R426}$
Dissociation constant (K_D) (μM)	56 ± 3	10 ± 1
Enthalpy (ΔH) (kcal/mol)	-7.7 ± 0.1	-5.0 ± 0.1
Entropy (TΔS) (kcal/mol)	-1.9 ± 0.2	+1.9 ± 0.1
Binding site size (n) (nucleotides)	6.5 ± 0.1	5.2 ± 0.1

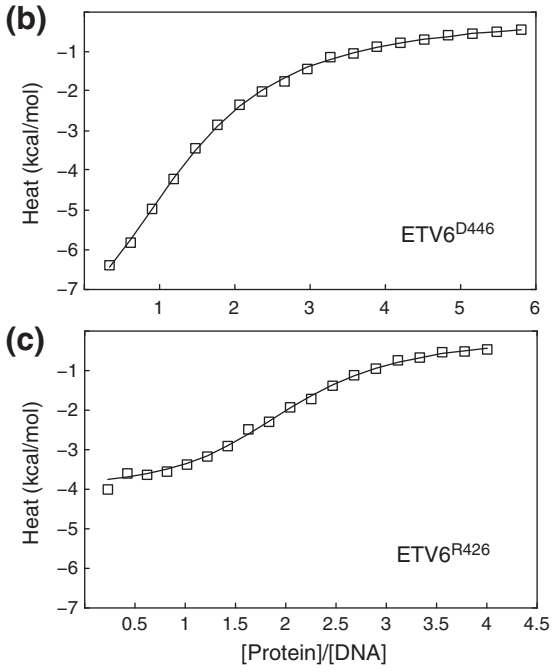

Fig. 4. Binding to non-specific DNA is also auto-inhibited. (a) Summary of the fit ITC data for DNA^{nonsp}, along with the binding isotherms for (b) inhibited $ETV6^{D446}$ and (c) uninhibited $ETV6^{R426}$. Raw data are open squares and the best fits to the Record model [23] are continuous lines.

DNA^{nonsp} relative to DNA^{sp}. We hypothesize that these spectral differences reflect looser, dynamic electrostatic interactions and the lack of direct base contacts in the non-specific DNA complex *versus* the specific complex. Consistent with this notion, the ^{15}N-NOE values for residues in the turn of the helix(H2)–turn–helix(H3) are slightly lower for $ETV6^{D446}$ bound to DNA^{nonsp} than to DNA^{sp}, indicating greater fast timescale mobility (Fig. 2c and d).

Insights into the binding interface from structures of free and DNA-bound $ETV6^{R426}$

To relate the abovementioned findings with the atomic details of the ETV6 binding interface, we used X-ray crystallography to determine the structure of its ETS domain bound to DNA. Since disordered regions are not conducive to crystallization and our NMR measurements clearly demonstrated that residues following Arg426 are unstructured in the ETV6–DNA^{sp} complex, we used $ETV6^{R426}$ for these studies. The crystal structure of this construct bound to a 14-bp specific $DNA^{sp\text{-}cryst}$ sequence (Table 1) was solved at 2.2 Å resolution (Table 3 and Fig. 6a). In parallel, we also used NMR spectroscopy to determine the structural ensemble of free $ETV6^{R426}$ (Table 2 and Fig. 3b). Other than the absence of the folded inhibitory helix H5, the structures of $ETV6^{R426}$ in its free and $DNA^{sp\text{-}cryst}$-bound states closely resemble those determined previously [16] for free inhibited $ETV6^{R458}$ with an average rmsd of 1.1 Å and 0.9 Å between all corresponding main-chain atoms for ordered residues, respectively. Therefore, neither the inhibitory helix H5 nor the DNA measurably alter the average structure of the ETV6 ETS domain. A similar lack of any significant backbone structural changes has been observed for other ETS proteins in their free *versus* bound states [2].

The contacts observed in the $ETV6^{R426}$–$DNA^{sp\text{-}cryst}$ interface, as summarized in Fig. 6b–f, are highly conserved in the ETS family [25]. Direct major groove base readout is mediated by bidentate hydrogen bonding of the invariant Arg392 and Arg395 in the recognition helix H3 to the G_{+2} and G_{+1} of the core $^{5'}$GGA$^{3'}$ motif, respectively. In most ETS factors, a tyrosine side chain in helix H3 hydrogen bonds to A_{+3}. However, the corresponding residue in ETV6 is His396, which is unable to provide this interaction. Rather, the specificity toward A_{+3} is determined via the complementary base $T_{+3'}$. The methyl group of $T_{+3'}$ occupies a hydrophobic pocket formed by the side chains of Arg392 and Lys389 (Fig. 6d). This hydrophobic interaction, which is also observed in other ETS domain–DNA structures, allows the Arg392 side chain to adopt the correct rotameric state required to hydrogen bond with the base G_{+2} and thus influences the overall specificity toward the core $^{5'}$GGA$^{3'}$ motif. The side chain of Glu388 also forms direct and water-mediated hydrogen bonds with the amino groups of C_{-2} and C_{-1}, respectively, thereby establishing the preference of ETV6 for cytosines at these positions [3]. Several residues also interact with the phosphodiester backbone of the DNA. The amide NH of Leu337 in helix H1 and Trp376 in helix H2 form highly conserved hydrogen bonds with the phosphate backbone. Residues Lys380 and Arg382 in the turn, Lys389 in H3 and Lys405 and Arg410 in the wing interact electrostatically with phosphate groups. These interactions may provide some specificity in the form of indirect shape readout [29] or may be relatively non-specific and simply increase the net affinity of ETV6 for DNA.

Histidine 396 determines specificity toward adenine at the +4 position

Most ETS factors can recognize either adenine or thymine at the +4 position in the core $^{5'}$GGA(A/T)$^{3'}$ sequence [3,30,31]. In contrast, based on qualitative

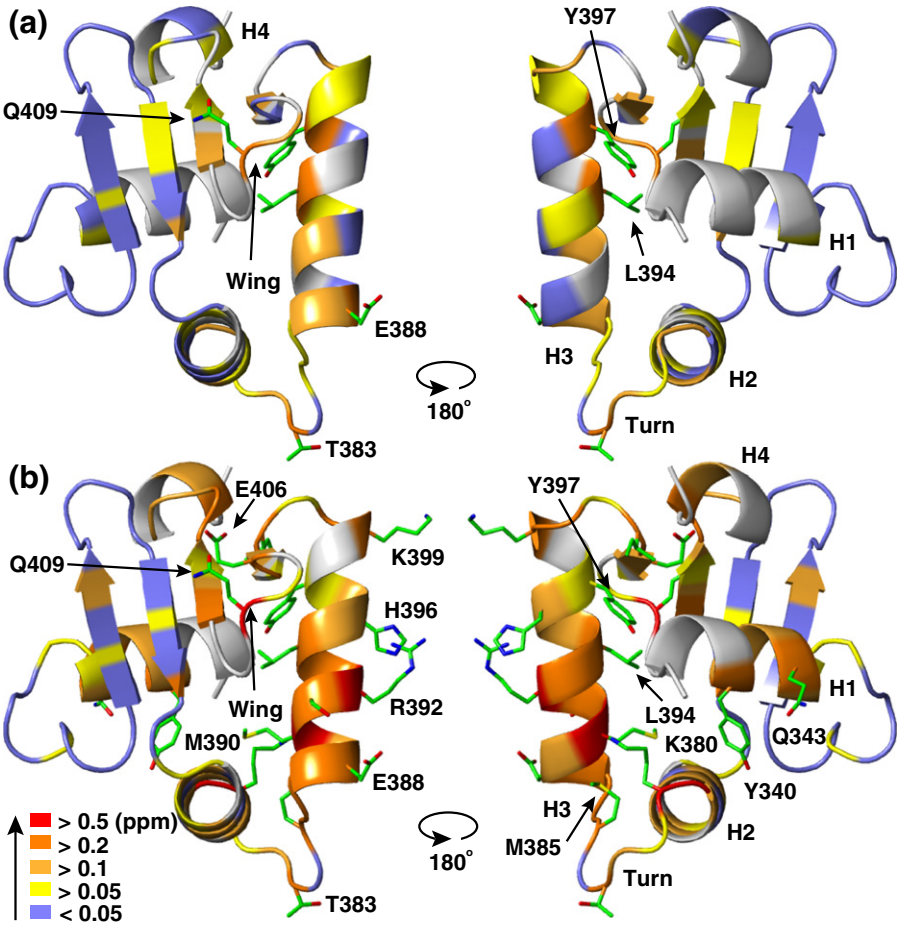

Fig. 5. ETV6 ETS domain binds specific and non-specific DNA via the same canonical interface. The amide CSPs ($\Delta\delta = \{\Delta\delta_H^2 + (0.154\Delta\delta_N)^2\}^{1/2}$) for (a) ETV6^{D446}–DNA^{nonsp} and (b) ETV6^{D446}–DNA^{sp} with respect to unbound ETV6^{R426} are mapped onto the crystal structure of ETV6^{R426}–DNA$^{sp\text{-}cryst}$ (DNA not shown). Residues (backbone cartoon) are colorcoded in the indicated CSP ranges. Prolines and unassigned residues are in gray. Side chains are shown for residues in (a) with CSP > 0.2 ppm and in (b) with CSP > 0.4 ppm. See Fig. 1 and Supplemental Figs. S1 and S4 for the original data.

high-throughput binding assays, ETV6 appears to have a distinct preference for adenine at this position [3]. This specificity has been hypothesized to arise from the presence of a non-conserved histidine in helix H3 of ETV6, rather than the more commonly found tyrosine. To confirm these observations, we used an electrophoretic mobility shift assay (EMSA) to measure the K_D values of ETV6^{D446} for DNA-binding sites with either a $^{5'}$GGAA$^{3'}$ or a $^{5'}$GGAT$^{3'}$ core sequence (Supplemental Fig. S6). Strikingly, ETV6^{D446} displayed 500-fold higher affinity toward the $^{5'}$GGAA$^{3'}$-bearing site (K_D values of 1.6 ± 0.3 nM *versus* 800 ± 100 nM). Mutating His396 to a tyrosine reduced this selectivity to only 8-fold (1.9 ± 0.3 nM *versus* 16 ± 7 nM). Given that both WT (*w*ild *t*ype) and H396Y-ETV6^{D446} bound the $^{5'}$GGAA$^{3'}$ oligonucleotide with very similar affinities, the presence of His396 strongly disfavors interactions with a thymine base at the +4 position.

The crystal structure of the ETV6^{R426}–DNA$^{sp\text{-}cryst}$ complex provides an explanation for this sequence specificity. As illustrated in Fig. 6f, His396 N$^{\varepsilon 2}$ is within hydrogen-bonding distance (2.8 Å) of the O_4 of $T_{+4'}$ on the DNA strand complementary to the $^{5'}$GGAA [3]. To act as a hydrogen bond donor, the side chain of His396 must be in the positively charged imidazolium or neutral N$^{\varepsilon 2}$H imidazole tautomeric state. When we modeled the A-T nucleotide pair to T-A at position +4, neither base at this position (T_{+4} or $A_{+4'}$) can form alternative hydrogen bonds with His396, unless perhaps it adopts the less favored neutral N$^{\delta 1}$H tautomer (Supplemental Fig. S7). In contrast, as shown by crystallographic studies of the ETS protein ELK4, the more common tyrosine can hydrogen bond with an adenine in either the +4 or the +4′ position [32]. Selectivity for the +4 base has also been observed for the ETS factors PU.1 and PDEF, which have Asn and Gln at the His396 equivalent position,

Table 3. Data collection and refinement statistics for $ETV6^{R426}$–$DNA^{cryst\text{-}sp}$

Data collection	
Space group	$P3_121$
Cell dimensions	
a, *b*, *c* (Å)	57.58, 57.58, 130.48
α, β, γ (°)	90, 90, 120
Resolution (Å)	50.00–2.20 (2.24–2.20)
R_{sym} or R_{merge}	0.085 (0.711)
$I/\sigma I$	29.13 (4.34)
Completeness (%)	99.6 (100.0)
Redundancy	7.9 (8.1)
Refinement	
Resolution (Å)	26.34–2.20
No. of reflections	13,290
R_{work}/R_{free}	0.175/0.221
No. of atoms	
Protein	813
DNA	590
Water	124
B-factors (Å^2)	
Overall (Wilson)	47.5 (37.9)
Protein	46.1
DNA	48.9
Water	49.6
rmsd	
Bond lengths (Å)	0.006
Bond angles (°)	1.32

respectively [3]. This arises as the Asn and Gln side chains of PU.1 and PDEF form water-mediated hydrogen bond with the $T_{+4'}$ and $A_{+4'}$ bases, respectively [33–35]. In contrast, His396 in ETV6 forms a hydrogen bond directly with the $T_{+4'}$ base.

Discussion

Steric mechanism of ETV6 auto-inhibition

In this study, we have extended our structural and thermodynamic understanding of the molecular basis of ETV6 auto-inhibition. Initially, we discovered that the CID attenuates specific DNA binding by ~50-fold [15]. Subsequently, we reported that the CID includes two helices, of which helix H5 packs along the canonical ETS domain DNA-binding interface [16]. This immediately predicted that substantial conformational changes must occur in ETV6 to enable its association with DNA. Alternatively, ETV6 might utilize a non-canonical mode of DNA binding, distinct from that of most ETS proteins. Although wHTH proteins typically contact DNA via the recognition helix H3, several different binding mechanisms have been identified [36]. Using both NMR spectroscopy and X-ray crystallography, we clearly demonstrated that ETV6 binds specific DNA via the canonical ETS domain interface. Furthermore, multiple lines of experimental evidence, including random coil chemical shifts, low ^{15}N-NOE values and high structural rmsd, prove that residues forming the inhibitory helix H5 undergo a folded-to-unfolded conformational change in order to form the DNA-bound state. These data also exclude alternative models such as the displacement of the folded helix to a non-inhibitory position. Collectively, this leads to a simple steric mechanism of auto-inhibition in which helix H5 and DNA compete in a mutually exclusive manner for the DNA-binding interface of ETV6. Importantly, amide hydrogen exchange studies revealed that helix H5 is only marginally stable and thus poised to unfold [16]. Through thermodynamic linkage, the modest energetic penalty of the requisite unfolding of this helix contributes to the net ~50-fold reduction of overall DNA affinity.

In addition to occluding the DNA-binding interface of ETV6, helix H5 also suppresses millisecond-to-microsecond timescale dynamics in the ETS domain [16]. Given that the structures of the ETS domain in ETV6 fragments with or without the inhibitory helix H5 are similar in both the free and DNA-bound states, these motions likely reflect small-scale excursions about a common average conformation. This structural plasticity is hypothesized to be a central feature along the protein–DNA recognition pathway, as exemplified by the well-studied lac and CAP repressors [37–39]. Although experimentally challenging, delineating the precise roles played by ETV6 backbone and side-chain mobility in both DNA binding and its auto-inhibition by the CID is an important future objective.

Non-specific DNA binding and its auto-inhibition

Sequence-specific DNA-binding proteins also have significant affinity for non-specific sequences. In a living cell, such non-specific sites outnumber the specific sites by many orders of magnitude. Although this poses a severe challenge for these proteins to locate their target sites, non-specific binding also greatly helps in this process both by buffering the concentration of free protein and by "facilitated target location" [40,41]. Experimental and theoretical studies indicated that, upon initially encountering a non-specific site, a protein will undergo sliding (one-dimensional diffusion) along the DNA, combined with direct transfer or jumping (three-dimensional diffusion after transient dissociation) between DNA segments in order to search for its specific, high-affinity target sites [42–47].

A growing number of proteins bound to non-cognate DNA sequences have been characterized by X-ray crystallography (e.g., steroid receptors [48,49], cro repressor [50], MATα2 homeodomain [51], several restriction enzymes [52–54] and Dam methyltransferase [55]) and NMR spectroscopy (e.g., lac repressor [37,38], a HMG-box protein [27], HoxD9 homeodomain [42,56], the bipartite Oct1 [45], papillomavirus E2 [57] and the Egr-1 [46] and ZNF217 [46] zinc fingers). In each of these

cases, the same approximate interface is utilized to bind both non-specific and specific DNA. However, at a more detailed level, there are necessarily differences in precise intermolecular orientation, protein–DNA contacts, buried surface area and so forth that account for the differences in affinity, and hence specificity, toward various DNA sequences. Broadly speaking, the interaction of sequence-specific DNA-binding proteins with non-specific DNA results primarily from electrostatic interaction between the positively-charged side chains of the protein and the negatively-charged DNA backbone [37,53]. It is also postulated that non-specific complexes are relatively dynamic with a high degree of hydration [49,58] and significant backbone and side-chain motions [37,38,45,46,56] that aid in the

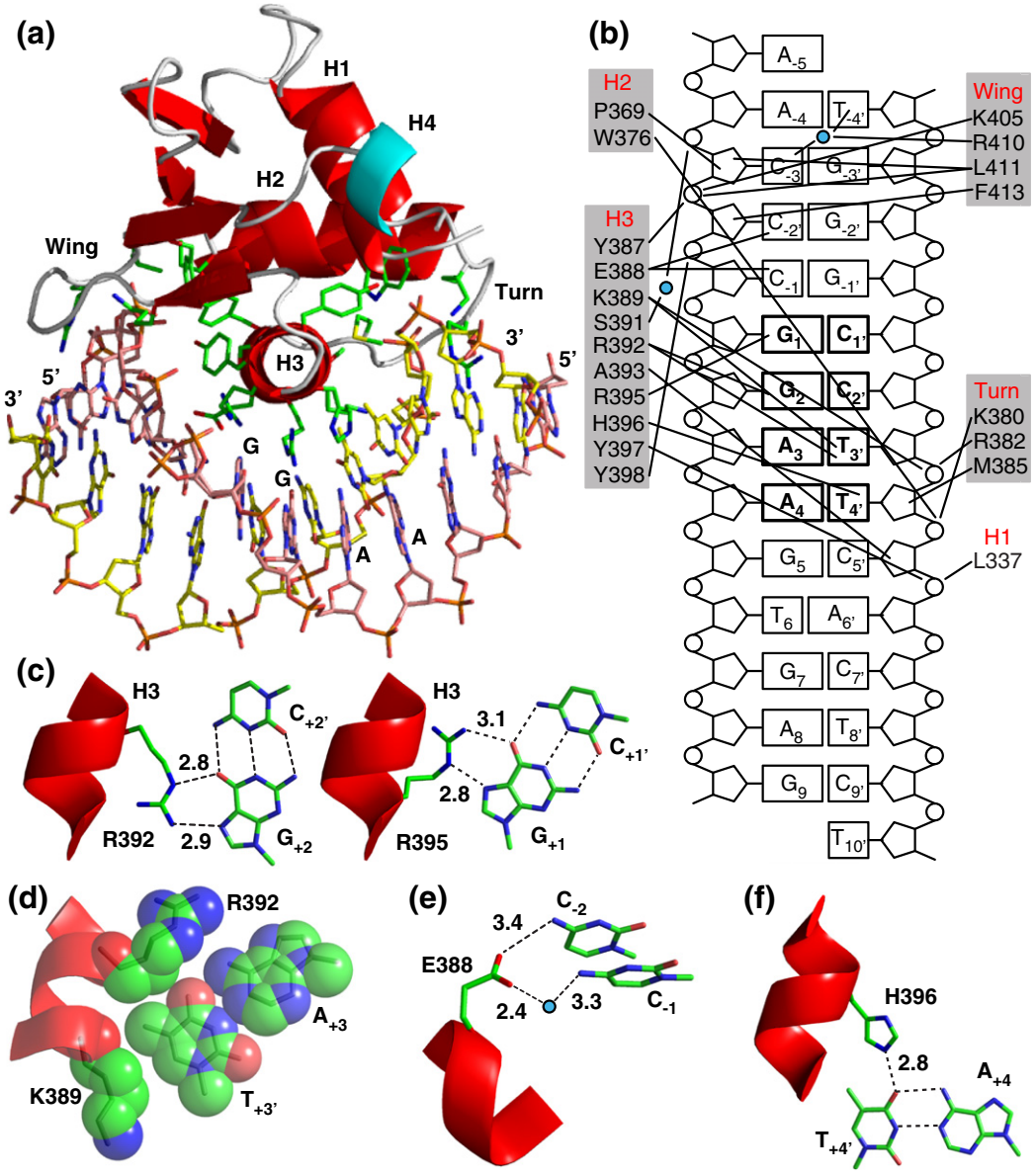

Fig. 6. Binding interface of ETV6^{R426}–DNA$^{sp\text{-}cryst}$ complex. (a) Crystal structure of the ETV6^{R426}–DNA$^{sp\text{-}cryst}$ complex. ETS domain residues contacting the DNA are shown in stick representation. Secondary structural elements in the core ETS domain are colored red, loops are in gray and helix H4 is in cyan. Corresponding backbone atoms for ordered residues in the crystal ETV6^{R426}–DNA$^{sp\text{-}cryst}$ and solution ETV6^{R426}–DNA^{sp} complexes superimposed with an average rmsd of 1.0 Å (data not shown). (b) Interfacial interactions with ETV6 residues grouped according to their secondary structure. Water molecules are denoted as blue circles. (c) Direct readout due to the invariant Arg392 and Arg395 interacting with G_{+2} and G_{+1}, respectively. (d) The methyl group on $T_{+3'}$ fits a small hydrophobic pocket created by the Arg392 and Lys389 side chains. (e) Glu388 interacts with the C_{-1} and C_{-2} bases. (f) Hydrogen bond between His396 and $T_{+4'}$ provides specificity toward the A_{+4} of the $^{5'}$GGAA$^{3'}$ motif (Supplemental Fig. S7). [In (c)–(f): carbon, green; oxygen, red; nitrogen, blue.]

efficient scanning for a target sequence. Once the cognate site is located, the protein and DNA undergo conformational changes leading to tight base-specific interactions [59–61].

We have characterized the interaction of the ETV6 ETS domain with a non-specific DNA oligonucleotide that lacks the $^{5'}$GGAA$^{3'}$ motif. Consistent with their relative affinities, NMR-monitored titrations show that specific and non-specific interactions are in slow ($k_{ex} < \Delta\omega$) and fast ($k_{ex} > \Delta\omega$) exchange regimes, respectively, where k_{ex} is the exchange rate constant ($k_{ex} = k_{on}[DNA] + k_{off}$) and $\Delta\omega$ is the difference in chemical shifts between the free and bound states of ETV6. The faster exchange with non-specific DNA likely reflects a shorter lifetime ($1/k_{off}$) of the bound state, as would be required for rapid target location. Conversely, the longer lifetime of the specific ETV6–DNA complex at regulatory sites would enable subsequent transcriptional repression. NMR chemical shift measurements confirm that ETV6 binds both specific and non-specific sequences using the same canonical ETS domain interface. However, the non-specific complex appears relatively loose, with weaker, dynamic time-averaged interactions. This conclusion is based on the three to four orders of magnitude higher K_D values of various ETV6 constructs for non-specific versus specific DNA's, along with the the general pattern of amide $^{1}H^{N}$ and ^{15}N chemical shifts changing in the same direction, yet with smaller magnitudes, upon binding DNA^{nonsp} *versus* DNA^{sp}. Since the ETV6 backbone structure is similar in both complexes, switching from a non-specific to specific complex likely involves conformational rearrangements of amino acid side chains in the binding interface without any significant global changes.

We also discovered that the non-specific DNA binding by ETV6 is auto-inhibited and accompanied by the unfolding of helix H5. This is consistent with the need to remove the steric blockage of the ETS domain interface. However, non-specific binding is only attenuated by ~5-fold, whereas specific DNA binding is auto-inhibited by ~50-fold. This may reflect a contribution of weak non-specific DNA binding via a non-canonical interface not occluded by the CID [51]. To the best of our knowledge, this is the first instance where auto-inhibition has been quantified for non-specific DNA binding. However, previous circular dichroism spectroscopic studies had indicated helical unfolding of ETS-1 upon binding to both specific and non-specific DNA [62]. Thus, auto-inhibition of non-specific DNA binding is likely a general feature of sequence-specific regulatory proteins such as those of the ETS family.

ETV6 exemplifies further diversity of ETS family auto-inhibitory mechanisms

Although auto-inhibition of DNA binding has been reported for several ETS proteins [2], detailed molecular mechanisms have only been elucidated for ETS-1, ERG and, now, ETV6. In the case of ETS-1, unfolding of its helical inhibitory module is linked allosterically to DNA binding. Furthermore, transient "fuzzy" interactions [63] by an adjacent disordered SRR increases auto-inhibition in a phosphorylation-dependent manner [6,9]. Auto-inhibition by a flexible sequence in ERG appears akin to that of the SRR in ETS-1 [10]. In contrast, ETV6 lacks N-terminal inhibitory sequences and contains a helical CID that sterically blocks its ETS domain. Although structurally distinct, ETS-1 and ETV6 auto-inhibition also share several common features, including coupled unfolding of a marginally stable helix with DNA binding and dampening of ETS domain dynamics by the appended inhibitory sequences. The latter dynamic changes were also reported to occur with ERG [10].

ETS-1 activity is regulated both positively and negatively via auto-inhibition. In particular, the effect is progressively reinforced due to increasing levels of SRR phosphorylation in response to Ca^{2+} signaling [6]. Conversely, cooperative DNA binding with partner transcription factors, such as RUNX1 [4] and Pax-5 [5], relieves auto-inhibition. Although the cellular control of ETV6 is less well characterized, it is reasonable to hypothesize that the CID could also integrate signaling pathways and protein partnerships to modulate DNA binding. Also, the self-association of ETV6 via its PNT domain may compensate for auto-inhibition through cooperative DNA binding to tandem ETS sites [15]. The mechanistic insights presented in this manuscript provide a foundation for understanding such potential roles of auto-inhibition in regulating transcriptional repression by ETV6.

Materials and Methods

Protein expression and purification

Three murine ETV6 fragments, with the sole cysteine (Cys334) mutated to serine, were used in this study: ETV6^{R426} (Gly329–Arg426), ETV6^{D446} (Gly329–Asp446) and, for preliminary experiments, ETV6$^{D446'}$ (Arg335–Asp446) lacking the first six residues (Table 1). These proteins differ from the previously characterized ETV6^{R458} (Arg335–Arg458) by the exact N-terminal sequence and by the deletion of unstructured residues C-terminal to helix H5 [16]. Genes encoding the ETV6 fragments were cloned in pET28b+ vectors and expressed in *Escherichia coli* BL21 (λDE3) cells. For $^{15}N/^{13}C$ labeling, we grew cell cultures in M9 minimal media supplemented with 1 g/L $^{15}NH_4Cl$ and 3 g/L $^{13}C_6$-glucose (or $^{13}C_6/D_7$-glucose for perdeuterated protein) as the sole nitrogen and carbon source, respectively. For perdeuterated and fractionally deuterated samples, cultures were grown in 99% and 70% D_2O M9 media, respectively. After induction for 6 h at 30 °C, cells were lysed by sonication in the presence of 4 M guanidinium HCl (H_2O). This denaturation step improved net yield and allowed complete back-exchange of the amide protons in

the deuterated samples. The His_6-tagged proteins were purified by Ni^{2+} affinity chromatography with on-column refolding before elution. After thrombin cleavage of the His_6-tag, the non-native N-terminal residues Gly-Ser-His-Met remained. Using gel-filtration chromatography (Superdex 75), we further purified and exchanged the proteins into final sample buffer (20 mM sodium phosphate, 50 mM NaCl, pH 6.5). Protein concentrations were determined by UV absorption using predicted molar absorptivity ε_{280} values [64].

DNA samples for NMR, ITC and crystallographic studies

DNA oligonucleotides were purchased from Integrated DNA Technologies and Sigma-Aldrich (without HPLC purification). Double-stranded DNA duplexes were generated by mixing the relevant single strands at equimolar ratio (determined from predicted molar absorptivity ε_{260} values), heating to 100 °C for 5 min and slowly cooling to room temperature. For NMR and ITC titration experiments, gel-filtration chromatography was used to purify and buffer exchange the resulting duplex DNA duplexes. For crystallographic studies, the preformed 1:1 protein–DNA complex was purified by gel-filtration chromatography.

NMR spectroscopy

NMR experiments were performed using TCI-cryoprobe-equipped Bruker Avance III 500, 600 and 850 MHz spectrometers at 25 °C. The proteins were 0.3–0.6 mM in sample buffer (20 mM phosphate, 50 mM NaCl, pH 6.5) with 6% lock D_2O. The collected spectra were processed and analyzed using NMRPipe [65] and Sparky [66], respectively. Signals from the ^{1}H, ^{13}C and ^{15}N nuclei in the backbone of $^{13}C/^{15}N$-labeled $ETV6^{D446}$ and the backbone and side chains of $^{13}C/^{15}N$-labeled $ETV6^{R426}$ were assigned using standard heteronuclear scalar correlation experiments [67]. Protein signals from DNA^{sp} complexes of amide-protonated $^{13}C/^{15}N$-labeled $ETV6^{D446}$ with uniformly deuterated, randomly factional (70%) deuterated or fully protonated side chains were assigned using experiments based on transverse relaxation optimized spectroscopy (TROSY) [68]. To ensure saturation, we present the DNA^{sp} in a 1.1-fold molar excess. Protein signals for the $ETV6^{D446}$–DNA^{nonsp} complex were assigned using ^{15}N-HSQC spectra to monitor the titration of the ^{15}N-labeled $ETV6^{D446}$ (initial, 0.2 mM; final, 0.15 mM) with aliquots of a 1.8 mM stock solution of DNA^{nonsp} in sample buffer. The molar ratios of DNA^{nonsp} to $ETV6^{D446}$ in the titration set were 0, 0.1, 0.25, 0.5, 0.75, 1, 2 and 3, yielding a final protein saturation of ~98% based on the data of Fig. 4. Binding occurred in the fast exchange limit; thus, amide $^{1}H^{N}$ and ^{15}N assignments were obtained by tracking shifts relative to the initial free $ETV6^{D446}$, and ^{13}C assignments were then determined from standard $^{1}H/^{13}C/^{15}N$ correlation spectra of the saturated complex.

Amide ^{15}N relaxation

Amide ^{15}N relaxation data (T_1, T_2 and heteronuclear NOE) [69] were collected for the specific complex of perdeuterated $ETV6^{D446'}$ and DNA^{sp} at 25 °C with a 600 MHz NMR spectrometer. Relaxation rate constants were determined with Sparky [66] by fitting the peak heights to an exponential decay. Heteronuclear $\{^{1}H\}$–^{15}N NOE data were also collected for ^{15}N-labeled $ETV6^{D446}$ complexed with DNA^{nonsp}. The ^{15}N-NOE value was determined from the ratio of the peak heights *versus* a control reference spectrum without ^{1}H saturation. The global tumbling correlation time for the specific complex was calculated using Tensor2 [21].

NMR structure calculations

NOE-derived distance restraints for $^{13}C/^{15}N$-labeled $ETV6^{R426}$ and $ETV6^{D446}$–DNA^{sp} were obtained by simultaneous three-dimensional ^{1}H–$^{15}N/^{13}C$–^{1}H NOE spectroscopy (NOESY)–HSQC (aliphatic/aromatic; τ_{mix} = 110 ms) and constant time methyl-methyl and amide-methyl $^{15}N/^{13}C$–^{13}C–^{1}H NOESY spectra (τ_{mix} = 100 ms) [70,71]. The NMR-derived structure ensembles of $ETV6^{R426}$ and the $ETV6^{D446}$–DNA^{sp} complex (protein only) were calculated using CYANA 3.0 [72] with chemical shift assignments, dihedral angle restraints from TALOS+ [73], NOESY cross-peaks and manually assigned methyl-methyl distance restraints as input data (Table 2). Structure calculations, combined with automated NOESY spectra assignments, were performed in seven iterative steps each yielding 100 structures. The 10 lowest-energy structures from the final step were further refined with CNS using explicit solvent and molecular dynamics simulations [74]. Although present in the $ETV6^{D446}$–DNA^{sp} complex, the signals from nuclei in DNA^{sp} were not assigned and its coordinates were not included in these calculations. Given this lack of chemical shift assignments, any intermolecular NOEs between $ETV6^{D446}$ and DNA^{sp} in the input NOESY cross-peak list were thus discarded by CYANA. Secondary structure boundaries were determined using DSSP and figures rendered with PyMOL [75].

Crystallization and structure determination

Low-salt buffer containing 20 mM Hepes and 50 mM NaCl at pH 7.5 was used for crystallization. $ETV6^{R426}$ was mixed with $DNA^{cryst\text{-}sp}$ in 1:1.1 molar ratio, and the resulting complex was purified by gel-filtration chromatography. The purified $ETV6^{R426}$–$DNA^{cryst\text{-}sp}$ was concentrated to ~0.3 mM. Crystallization trials were carried out by the hanging-drop vapor diffusion method using 1 mL reservoir solution of 50 mM sodium cacodylate, 100 mM ammonium acetate, 10 mM $MgCl_2$ and 22% polyethylene glycol 8000 at pH 6.0 and a mixture of 2 μL complex and 2 μL of well solution. Crystals were obtained at room temperature within 5–7 days.

$ETV6^{R426}$–$DNA^{cryst\text{-}sp}$ crystals were soaked stepwise for a few seconds each in mother liquor supplemented with 5% and 10% polyethylene glycol 8000 and were flash frozen using liquid nitrogen. A 2.2-Å resolution dataset was collected at 100 K using the Stanford Synchrotron Radiation Lightsource beamline 7–1 with 0.9753 Å incident radiation. After data processing with HKL2000 [76], we used MOLREP [77] for initial phase determination using the coordinates of the Elk-1 ETS domain (Protein

Data Bank ID: 1DUX) as a starting model. Cycles of structure refinement and building were performed using PHENIX [78], Refmac 5 [79] from the CCP4 suite of programs [80] and Coot [81]. Water molecules were automatically added using PHENIX and manually corrected. The crystal structure of ETV6^{R426}–DNA$^{cryst\text{-}sp}$ was determined in space group $P3_12_1$ with one monomer in the asymmetric unit. Sufficient electron density was observed to build residues 335–424 of ETV6^{R426} and the full duplex oligonucleotide. Ramachandran statistics indicated excellent stereochemistry with 98.8% of residues in the preferred region and no outliers. Data collection and refinement statistics are listed in Table 3.

Isothermal titration calorimetry

ITC measurements were performed at 25 °C with a Microcal ITC200. The protein and DNA samples were buffer-exchanged by gel filtration into 20 mM sodium phosphate and 50 mM NaCl at pH 6.5. Titrations were carried out with 20 μM DNA^{nonsp} in the 200-μL reaction cell and 2 μL injections of ETV6^{D446} (0.58 mM) or ETV6^{R426} (0.40 mM) at 3-min intervals for a total of 20 injections. Heat of dilutions, measured by titrating proteins into buffer and buffer into DNA, was subsequently subtracted from the respective titration experiments. The binding of ETV6 fragments to non-specific DNA was analyzed using the Record model [23] as described by equations [1–3]

$$\frac{v_{NS}}{[L]} = K_A(1-nv_{NS})\left(\frac{1-nv_{NS}}{1-(n-1)v_{NS}}\right)^{n-1}\left(\frac{N-n+1}{N}\right) \quad (1)$$

The non-specific binding density v_{NS} is $[ETV6]_{bound}$/[total DNA bp], [L] is $[ETV6]_{free}$, K_A is the average microscopic association constant to any potential DNA site, n is the number of DNA base pairs bound by the protein and N is the total base pairs in the oligonucleotide. In the ITC experiments, the heat content Q_i after each injection "i" is given by:

$$Q_i = v_{NS,i}[\text{total DNA bp}]\Delta H^{\circ} V_{\circ} \quad (2)$$

The reaction cell volume is V_o, binding enthalpy is ΔH^o and binding density after injection "i" is $v_{NS,i}$. The differential heat ΔQ_i measured by the ITC instrument is given by:

$$\Delta Q_i = Q_i + \frac{V_i}{V_{\circ}}\left[\frac{Q_i + Q_{i-1}}{2}\right] - Q_{i-1} \quad (3)$$

The ITC binding isotherms were fit to these equations with Matlab. Errors in each fitted parameter were estimated from Monte Carlo simulations.

Accession numbers

The chemical shift assignments of ETV6^{R426} have been deposited in the Biological Magnetic Resonance Bank ID 19474. The atomic coordinates of ETV6^{R426} and ETV6^{R426}–DNA$^{cryst\text{-}sp}$ have been deposited in Protein Data Bank IDs 2MD5 and 4MHG, respectively.

Acknowledgements

This study was funded by the Canadian Cancer Society Research Institute (CCSRI 2011–700772 to L.P.M.) and the National Institutes of Health (R01GM38663 to B.J.G.). Instrument support was provided by the Canadian Institutes for Health Research, the Canada Foundation for Innovation, the British Columbia Knowledge Development Fund, the UBC Blusson Fund and the Michael Smith Foundation for Health Research. Funding from the Huntsman Cancer Institute/Huntsman Cancer Foundation is also acknowledged. Portions of this research were carried out at the Stanford Synchrotron Radiation Lightsource, a Directorate of Stanford Linear Accelerator Center National Accelerator Laboratory and an Office of Science User Facility operated for the U.S. Department of Energy Office of Science by Stanford University. The Stanford Synchrotron Radiation Lightsource Structural Molecular Biology Program is supported by the Department of Energy Office of Biological and Environmental Research and by the National Institutes of Health, National Institute of General Medical Sciences (including P41GM103393) and the National Center for Research Resources (P41RR001209). The contents of this publication are solely the responsibility of the authors and do not necessarily represent the official views of National Institute of General Medical Sciences, National Center for Research Resources or National Institutes of Health.

Appendix A. Supplementary Data

Supplementary data to this article can be found online at http://dx.doi.org/10.1016/j.jmb.2013.11.031.

Received 18 September 2013;
Received in revised form 5 November 2013;
Accepted 9 November 2013
Available online 12 December 2013

Keywords:
inhibitory module;
helix unfolding;
protein–DNA interface;
ETS family;
winged helix–turn–helix

Abbreviations used:
ITC, isothermal titration calorimetry; SRR, serine-rich region; CSP, chemical shift perturbation; HSQC, heteronuclear single quantum correlation; NOE, nuclear Overhauser enhancement; wHTH, winged helix–turn–helix; NOESY, NOE spectroscopy.

References

[1] Pufall MA, Graves BJ. Autoinhibitory domains: modular effectors of cellular regulation. Annu Rev Cell Dev Biol 2002;18:421–62.

[2] Hollenhorst PC, McIntosh LP, Graves BJ. Genomic and biochemical insights into the specificity of ETS transcription factors. Ann Rev Biochem 2011;80:437–71.

[3] Wei GH, Badis G, Berger MF, Kivioja T, Palin K, Enge M, et al. Genome-wide analysis of ETS-family DNA-binding *in vitro* and *in vivo*. EMBO J 2010;29:2147–60.

[4] Goetz TL, Gu TL, Speck NA, Graves BJ. Auto-inhibition of Ets-1 is counteracted by DNA binding cooperativity with core-binding factor alpha2. Mol Cell Biol 2000;20:81–90.

[5] Fitzsimmons D, Lukin K, Lutz R, Garvie CW, Wolberger C, Hagman J. Highly cooperative recruitment of Ets-1 and release of autoinhibition by Pax5. J Mol Biol 2009;392:452–64.

[6] Pufall MA, Lee GM, Nelson ML, Kang HS, Velyvis A, Kay LE, et al. Variable control of Ets-1 DNA binding by multiple phosphates in an unstructured region. Science 2005;309:142–5.

[7] Garvie CW, Pufall MA, Graves BJ, Wolberger C. Structural analysis of the autoinhibition of Ets-1 and its role in protein partnerships. J Biol Chem 2002;277:45529–36.

[8] Lee GM, Donaldson LW, Pufall MA, Kang HS, Pot I, Graves BJ, et al. The structural and dynamic basis of Ets-1 DNA binding autoinhibition. J Biol Chem 2005;280:7088–99.

[9] Lee GM, Pufall MA, Meeker CA, Kang HS, Graves BJ, McIntosh LP. The affinity of Ets-1 for DNA is modulated by phosphorylation through transient interactions of an unstructured region. J Mol Biol 2008;382:1014–30.

[10] Regan MC, Horanyi PS, Pryor EE, Sarver JL, Cafiso DS, Bushweller JH. Structural and dynamic studies of the transcription factor ERG reveal DNA binding is allosterically autoinhibited. Proc Natl Acad Sci USA 2013;110:13374–9.

[11] Bohlander SK. ETV6: a versatile player in leukemogenesis. Semin Cancer Biol 2005;15:162–74.

[12] Kim CA, Phillips ML, Kim W, Gingery M, Tran HH, Robinson MA, et al. Polymerization of the SAM domain of TEL in leukemogenesis and transcriptional repression. EMBO J 2001;20:4173–82.

[13] Qiao F, Song HY, Kim CA, Sawaya MR, Hunter JB, Gingery M, et al. Derepression by depolymerization: structural insights into the regulation of Yan by Mae. Cell 2004;118:163–73.

[14] Zhang J, Graham TG, Vivekanand P, Cote L, Cetera M, Rebay I. Sterile alpha motif domain-mediated self-association plays an essential role in modulating the activity of the Drosophila ETS family transcriptional repressor Yan. Mol Cell Biol 2010;30:1158–70.

[15] Green SM, Coyne HJ, McIntosh LP, Graves BJ. DNA binding by the ETS protein TEL (ETV6) is regulated by autoinhibition and self-association. J Biol Chem 2010;285:18496–504.

[16] Coyne HJ, De S, Okon M, Green SM, Bhachech N, Graves BJ, et al. Autoinhibition of ETV6 (TEL) DNA binding: appended helices sterically block the ETS domain. J Mol Biol 2012;421:67–84.

[17] Shen Y, Bax A. Identification of helix capping and beta-turn motifs from NMR chemical shifts. J Biomol NMR 2012;52:211–32.

[18] Berjanskii MV, Wishart DS. A simple method to predict protein flexibility using secondary chemical shifts. J Am Chem Soc 2005;127:14970–1.

[19] Daragan VA, Mayo KH. Motional model analyses of protein and peptide dynamics using ^{13}C and ^{15}N NMR relaxation. Prog Nucl Magn Reson Spectrosc 1997;31:63–105.

[20] Lipari G, Szabo A. Model-free approach to the interpretation of nuclear magnetic resonance relaxation in macromolecules. 2. Analysis of experimental results. J Am Chem Soc 1982;104:4559–70.

[21] Dosset P, Hus JC, Blackledge M, Marion D. Efficient analysis of macromolecular rotational diffusion from heteronuclear relaxation data. J Biomol NMR 2000;16:23–8.

[22] McGhee JD, von Hippel PH. Theoretical aspects of DNA–protein interactions: co-operative and non-co-operative binding of large ligands to a one-dimensional homogeneous lattice. J Mol Biol 1974;86:469–89.

[23] Tsodikov OV, Holbrook JA, Shkel IA, Record MT. Analytic binding isotherms describing competitive interactions of a protein ligand with specific and nonspecific sites on the same DNA oligomer. Biophys J 2001;81:1960–9.

[24] Chaires JB. Analysis and interpretation of ligand-DNA binding isotherms. Methods Enzymol 2001;340:3–22.

[25] Grishin AV, Alexeevsky AV, Spirin SA, Karyagina AS. Conserved structural features of ETS domain-DNA complexes. Mol Biol 2009;43:612–9.

[26] Selvaratnam R, Mazhab-Jafari MT, Das R, Melacini G. The auto-inhibitory role of the EPAC hinge gelix as mapped by NMR. PLoS One 2012;7:e48707.

[27] Iwahara J, Schwieters CD, Clore GM. Characterization of nonspecific protein–DNA interactions by ^{1}H paramagnetic relaxation enhancement. J Am Chem Soc 2004;126:12800–8.

[28] Vandevenne M, Jacques DA, Artuz C, Nguyen CD, Kwan AHY, Segal DJ, et al. New insights into DNA recognition by zinc fingers revealed by structural analysis of the oncoprotein ZNF217. J Biol Chem 2013;288:10616–27.

[29] Rohs R, Jin X, West SM, Joshi R, Honig B, Mann RS. Origins of specificity in protein–DNA recognition. Annu Rev Biochem 2010;79:233–69.

[30] Szymczyna BR, Arrowsmith CH. DNA binding specificity studies of four ETS proteins support an indirect read-out mechanism of protein–DNA recognition. J Biol Chem 2000;275:28363–70.

[31] Poon GM, Macgregor RB. Base coupling in sequence-specific site recognition by the ETS domain of murine PU.1. J Mol Biol 2003;328:805–19.

[32] Mo Y, Vaessen B, Johnston K, Marmorstein R. Structures of SAP-1 bound to DNA targets from the E74 and c-fos promoters: insights into DNA sequence discrimination by Ets proteins. Mol Cell 1998;2:201–12.

[33] Kodandapani R, Pio F, Ni CZ, Piccialli G, Klemsz M, McKercher S, et al. A new pattern for helix-turn-helix recognition revealed by the PU.1 ETS-domain-DNA complex. Nature 1996;380:456–60.

[34] Wang Y, Feng L, Said M, Balderman S, Fayazi Z, Liu Y, et al. Analysis of the 2.0 Å crystal structure of the protein–DNA complex of the human PDEF ETS domain bound to the prostate specific antigen regulatory site. Biochemistry 2005;44:7095–106.

[35] Poon GM. Sequence discrimination by DNA-binding domain of ETS family transcription factor PU.1 is linked to specific

hydration of protein–DNA interface. J Biol Chem 2012;287:18297–307.
[36] Harami GM, Gyimesi M, Kovacs M. From keys to bulldozers: expanding roles for winged helix domains in nucleic-acid-binding proteins. Trends Biochem Sci 2013;38:364–71.
[37] Kalodimos CG, Biris N, Bonvin AM, Levandoski MM, Guennuegues M, Boelens R, et al. Structure and flexibility adaptation in nonspecific and specific protein–DNA complexes. Science 2004;305:386–9.
[38] Kalodimos CG, Boelens R, Kaptein R. Toward an integrated model of protein–DNA recognition as inferred from NMR studies on the Lac repressor system. Chem Rev 2004;104:3567–86.
[39] Tzeng SR, Kalodimos CG. Allosteric inhibition through suppression of transient conformational states. Nat Chem Biol 2013;9:462–5.
[40] von Hippel PH, Berg OG. Facilitated target location in biological systems. J Biol Chem 1989;264:675–8.
[41] Clore GM. Exploring translocation of proteins on DNA by NMR. J Biomol NMR 2011;51:209–19.
[42] Iwahara J, Clore GM. Detecting transient intermediates in macromolecular binding by paramagnetic NMR. Nature 2006;440:1227–30.
[43] Givaty O, Levy Y. Protein sliding along DNA: dynamics and structural characterization. J Mol Biol 2009;385:1087–97.
[44] Blainey PC, Luo GB, Kou SC, Mangel WF, Verdine GL, Bagchi B, et al. Nonspecifically bound proteins spin while diffusing along DNA. Nat Struct Mol Biol 2009;16:1224–34.
[45] Takayama Y, Clore GM. Intra- and intermolecular translocation of the bi-domain transcription factor Oct1 characterized by liquid crystal and paramagnetic NMR. Proc Natl Acad Sci USA 2011;108:E169–76.
[46] Zandarashvili L, Vuzman D, Esadze A, Takayama Y, Sahu D, Levy Y, et al. Asymmetrical roles of zinc fingers in dynamic DNA-scanning process by the inducible transcription factor Egr-1. Proc Natl Acad Sci USA 2012;109:E1724–32.
[47] Loth K, Gnida M, Romanuka J, Kaptein R, Boelens R. Sliding and target location of DNA-binding proteins: an NMR view of the lac repressor system. J Biomol NMR 2013;56:41–9.
[48] Luisi BF, Xu WX, Otwinowski Z, Freedman LP, Yamamoto KR, Sigler PB. Crystallographic analysis of the interaction of the glucocorticoid receptor with DNA. Nature 1991;352:497–505.
[49] Gewirth DT, Sigler PB. The basis for half-site specificity explored through a noncognate steroid receptor-DNA complex. Nat Struct Biol 1995;2:386–94.
[50] Albright RA, Mossing MC, Matthews BW. Crystal structure of an engineered Cro monomer bound nonspecifically to DNA: possible implications for nonspecific binding by the wild-type protein. Protein Sci 1998;7:1485–94.
[51] Aishima J, Wolberger C. Insights into nonspecific binding of homeodomains from a structure of MATalpha2 bound to DNA. Proteins 2003;51:544–51.
[52] Winkler FK, Banner DW, Oefner C, Tsernoglou D, Brown RS, Heathman SP, et al. The crystal structure of EcoRV endonuclease and of its complexes with cognate and non-cognate DNA fragments. EMBO J 1993;12:1781–95.
[53] Viadiu H, Aggarwal AK. Structure of BamHI bound to nonspecific DNA: a model for DNA sliding. Mol Cell 2000;5:889–95.
[54] Townson SA, Samuelson JC, Bao Y, Xu SY, Aggarwal AK. BstYI bound to noncognate DNA reveals a "hemispecific" complex: implications for DNA scanning. Structure 2007;15:449–59.
[55] Horton JR, Liebert K, Hattman S, Jeltsch A, Cheng X. Transition from nonspecific to specific DNA interactions along the substrate-recognition pathway of dam methyltransferase. Cell 2005;121:349–61.
[56] Iwahara J, Zweckstetter M, Clore GM. NMR structural and kinetic characterization of a homeodomain diffusing and hopping on nonspecific DNA. Proc Natl Acad Sci USA 2006;103:15062–7.
[57] Brown C, Campos-Leon K, Strickland M, Williams C, Fairweather V, Brady RL, et al. Protein flexibility directs DNA recognition by the papillomavirus E2 proteins. Nucleic Acids Res 2011;39:2969–80.
[58] Sidorova NY, Rau DC. Differences in water release for the binding of EcoRI to specific and nonspecific DNA sequences. Proc Natl Acad Sci USA 1996;93:12272–7.
[59] Marcovitz A, Levy Y. Frustration in protein–DNA binding influences conformational switching and target search kinetics. Proc Natl Acad Sci USA 2011;108:17957–62.
[60] Sanchez IE, Ferreiro DU, Dellarole M, de Prat-Gay G. Experimental snapshots of a protein–DNA binding landscape. Proc Natl Acad Sci USA 2010;107:7751–6.
[61] Zhou HX. Rapid search for specific sites on DNA through conformational switch of nonspecifically bound proteins. Proc Natl Acad Sci USA 2011;108:8651–6.
[62] Petersen JM, Skalicky JJ, Donaldson LW, McIntosh LP, Alber T, Graves BJ. Modulation of transcription factor Ets-1 DNA binding: DNA-induced unfolding of an alpha helix. Science 1995;269:1866–9.
[63] Fuxreiter M. Fuzziness: linking regulation to protein dynamics. Mol Biosyst 2012;8:168–77.
[64] Gasteiger E, Gattiker A, Hoogland C, Ivanyi I, Appel RD, Bairoch A. ExPaSy: the proteomics server for in-depth protein knowledge and analysis. Nucleic Acids Res 2005;31:3784–8.
[65] Delaglio F, Grzesiek S, Vuister GW, Zhu G, Pfeifer J, Bax A. NMRPipe: a multidimensional spectral processing system based on UNIX pipes. J Biomol NMR 1995;6:277–93.
[66] Goddard TD, Kneeler DG. Sparky. 3rd ed. San Francisco: University of California; 1999.
[67] Sattler M, Schleucher J, Griesinger C. Heteronuclear multidimensional NMR experiments for the structure determination of proteins in solution employing pulsed field gradients. Prog Nucl Magn Reson Spectrosc 1999;34:93–158.
[68] Yang D, Kay LE. Improved $^{1}H^{N}$-detected triple resonance TROSY-based experiments. J Biomol NMR 1999;13:3–10.
[69] Farrow NA, Muhandiram R, Singer AU, Pascal SM, Kay CM, Gish G, et al. Backbone dynamics of a free and phosphopeptide-complexed Src homology 2 domain studied by ^{15}N NMR relaxation. Biochemistry 1994;33:5984–6003.
[70] Pascal SM, Muhandiram DR, Yamazaki T, Formankay JD, Kay LE. Simultaneous acquisition of ^{15}N-edited and ^{13}C-edited NOE spectra of proteins dissolved in H_2O. J Magn Reson B 1994;103:197–201.
[71] Zwahlen C, Gardner KH, Sarma SP, Horita DA, Byrd RA, Kay LE. An NMR experiment for measuring methyl-methyl NOEs in ^{13}C-labeled proteins with high resolution. J Am Chem Soc 1998;120:7617–25.
[72] Guntert P. Automated NMR structure calculation with CYANA. Methods Mol Biol 2004;278:353–78.
[73] Shen Y, Delaglio F, Cornilescu G, Bax A. TALOS+: a hybrid method for predicting protein backbone torsion angles from NMR chemical shifts. J Biomol NMR 2009;44:213–23.
[74] Brunger AT, Adams PD, Clore GM, DeLano WL, Gros P, Grosse-Kunstleve RW, et al. Crystallography & NMR system: a

new software suite for macromolecular structure determination. Acta Crystallogr Sect D Biol Crystallogr 1998;54:905–21.
[75] DeLano WL. Use of PYMOL as a communications tool for molecular science. Abstr Pap Am Chem Soc 2004;228: U313–4.
[76] Otwinowski Z, Minor W. Processing of X-ray diffraction data. Methods Enzymol 1997;276:307–26.
[77] Vagin A, Teplyakov A. MOLREP: an automated program for molecular replacement. J Appl Crystallogr 1997;30:1022–5.
[78] Adams PD, Afonine PV, Bunkoczi GB, Chen VB, Davis IW, Echols N, et al. PHENIX: a comprehensive Python-based system for macromolecular structure solution. Acta Crystallogr Sect D Biol Crystallogr 2004;66:213–21.
[79] Murshudov GN, Vagin AA, Dodson EJ. Refinement of macromolecular structures by the maximum-likelihood method. Acta Crystallogr Sect D Biol Crystallogr 1997;53:240–55.
[80] Winn MD, Ballard CC, Cowtan KD, Dodson EJ, Emsley P, Evans PR, et al. Overview of the CCP4 suite and current developments. Acta Crystallogr Sect D Biol Crystallogr 2011;67:235–42.
[81] Emsley P, Cowtan K. Coot: model-building tools for molecular graphics. Acta Crystallogr Sect D Biol Crystallogr 2004;60:2126–32.